

<https://doi.org/10.1038/s43856-025-00925-4>

Computational and biological modeling of IGF1R inhibition for multifocal medulloblastoma



Alyssa G. Almer¹, Samuel V. Rasmussen¹ , Dina Kats¹, Matthew N. Svalina¹, Bonnie L. Cole², Mohammadreza Khani^{3,4}, Sonja Chen⁵, Samuel H. Cheshier⁶, Bryn A. Martin^{3,4}, Noah E. Berlow¹ & Charles Keller¹

Abstract

Background Leptomeningeal metastasis in medulloblastoma poses challenges for effective treatments due to the blood–brain barrier (BBB), which may be addressed through intrathecal or intraventricular drug delivery. However, the lack of pharmacokinetic modeling for pathological cerebrospinal fluid (CSF) geometries has limited the ability to predict effective intrathecal and intraventricular drug exposure.

Methods A patient-specific computational fluid dynamics “in silico” trial was conducted to simulate CSF movement to examine the tumor microenvironment in terms of drug–target exposure over time following intraventricular delivery via Omayia Reservoir. Simultaneously, we conducted cellular adhesion experiments to test the therapeutic potential of IGF1R inhibition on metastasis under patient-specific flow conditions generated by computational analysis.

Results A 3-dimensional computational fluid dynamics (CFD) model based on patient-specific conditions was obtained to predict an efficacious drug concentration, providing guidance for therapeutic drug exposure at targeted sites. Microfluidic experiments for IGF1R inhibition of cellular adhesion showed the potential for reduced attachment of medulloblastoma to leptomeningeal cells to prevent metastasis.

Conclusions This study offers insights from patient-specific in silico trials for the precision delivery of small-molecule drugs for the treatment of central nervous system (CNS) malignancies.

Plain language summary

Medulloblastoma is a fast-growing tumor in the brain that can be treated through several strategies. Tumor that has spread (metastatic) can be difficult to treat because many drugs cannot reach the tumor location, or the tumors obstruct drug exposure in the spinal fluid. We conducted proof-of-concept 3D dynamic fluid modeling using computers to determine how drugs would spread and be delivered. We then checked these findings with studies that mimicked a patient’s brain and tested the delivery of a specific drug. We found the drug could reach the target tumor in the simulation and help stop new metastasis formation, but did not impact existing metastases.

Medulloblastoma is the most common malignant brain tumor in children^{1–3}. Surgical resection, chemotherapy, and craniospinal radiation in standard-risk patients over 3 years of age results in a 5-year survival rate of over 80%⁴. Medulloblastoma has been stratified by transcriptional profiling into four main subgroups: wingless (WNT), sonic hedgehog (SHH), group 3, and group 4⁵. Group 3 medulloblastomas, especially with *MYC* amplification, portend a poor prognosis, with a survival rate of less than 50%⁶. Metastases are more prevalent in group 3 medulloblastomas compared to any other group, with a high propensity for metastasis to leptomeningeal tissues⁵. Medulloblastoma metastases to the leptomeningeal surface of the

brain and spinal cord are often refractory to treatment: patients with leptomeningeal metastasis, even with combined radiotherapy and intensive chemotherapy, face a 5-year survival rate of less than 30%⁷. Therefore, understanding the molecular and fluid transport mechanisms that drive migration and adhesion to the leptomeninges and drug delivery along the CNS axis could be beneficial for therapeutic interventions aimed at overcoming the mortality and morbidity of metastatic medulloblastoma.

As prophylaxis against metastases, irradiation of the entire brain and spinal cord in all patients over 3 years of age is both the standard of care and the major source of morbidity to survivors, resulting in severe detrimental

¹Children’s Cancer Therapy Development Institute, Hillsboro, OR, USA. ²Department of Pathology, Seattle Children’s Hospital, Seattle, WA, USA. ³Department of Biological Engineering, University of Idaho, Moscow, ID, USA. ⁴Alcyone Therapeutics, Inc., Lowell, MA, USA. ⁵Department of Pathology, Nationwide Children’s Hospital, Columbus, OH, USA. ⁶Division of Pediatric Neurosurgery, Department of Neurosurgery, Huntsman Cancer Institute, Intermountain Primary Children’s Hospital, University of Utah, Salt Lake City, UT, USA. e-mail: samuel@cc-tdi.org; charles@cc-tdi.org

effects on cognitive and endocrine function, as well as the development of secondary radiation-induced neoplasms⁷. No therapies are approved or in clinical trials for the specific treatment or prevention of medulloblastoma leptomeningeal metastases. Thus, a primary clinical challenge in the treatment of medulloblastoma is preventing leptomeningeal dissemination⁸.

Previously published studies from our lab⁹ found that insulin-like growth factor type 1 (IGF1) led to receptor phosphorylation and accelerated migration/adhesion in MYC-amplified medulloblastoma. Insulin-like growth factor type 1 receptor (IGF1R) is a tetrameric receptor consisting of two alpha subunits (which are extracellular and bind IGF) and two transmembrane beta subunits. Each transmembrane beta subunit contains an intracellular tyrosine kinase domain. The binding of IGF1 or IGF2 to IGF1R results in autophosphorylation of three key tyrosine residues in the receptor (leading to phosphorylation of downstream substrates). Pathways that have been well described include Grb2, which signals through Ras, Raf, and ultimately MAPK, leading to cell proliferation¹⁰.

Previously, three MYC-amplified medulloblastoma cell lines and one autopsy-derived medulloblastoma primary culture were tested against a chemical screen of 60 compounds and found to be consistently sensitive to IGF1R inhibitors⁹. The most potent of the three IGF1R inhibitors tested was BMS-754807, an IGF1R/InsR inhibitor. Svalina et al.⁹ identified IGF1R as a key target, whereas our goal here is to further investigate the role of IGF1R in leptomeningeal metastasis in a variety of models and to assess the efficacy and anti-metastatic activity of BMS-754807 as a potential therapeutic intervention in high-risk medulloblastoma.

In our research, we investigated the dispersion, penetration, and effects of BMS-754807 using *in silico*, *in vivo*, and *in vitro* modeling. The *in silico* modeling we conducted determined the dispersion of the compound added to the CSF to increase delivery to the tumor and metastasis that may have formed. The *in vivo* research determined that BMS-754807 can cross the blood–brain barrier to a degree. We conducted *in vitro* research showing the ability of BMS-754807 and IGF1 silencing to decrease the ability of medulloblastoma cells to attach under flow. We conducted additional microfluidic studies testing BMS-754807 on medulloblastoma cells attached to BMEN and did not find a significant effect vs control, showing that the compound may not have an effect on already formed metastasis.

Materials and methods

Cell lines

D425 has been previously reported¹¹ and was obtained from the Bigner Lab. D425 was cultured in Dulbecco's Modified Eagle Medium (DMEM) (cat#11965092, Thermo Fisher Gibco, Waltham, MA) containing 10% fetal bovine serum (FBS) (cat#10437036, Thermo Fisher Scientific), 1% L-glutamine (cat#10438034, Thermo Fisher Scientific), 1% penicillin/streptomycin (cat#15140122, Thermo Fisher Scientific), per manufacturer's instructions. DAOY, D341 Med¹², CHLA-01-MED, and CHLA-01R-MED were obtained from ATCC (HTB-186, HTB-187, CRL-3021, and CRL-3034, respectively; ATCC, Manassas, VA) and cultured according to the manufacturer's instructions. A culture of D425 cells was transfected with GFP (EF1a-Puro) lentiviral particles (cat#LVP426; GenTarget, San Diego, CA) to stably express GFP, per the manufacturer's instructions. This was followed by two courses of antibiotic selection and flow sorting for GFP+ cells using a BD FACSAria II (BD Bioscience, Franklin Lakes, NJ) to yield a 98% GFP+ culture of D425 (referred to as GFPsD425).

The human DAOY cell line used as a control with MYC-amplified cell lines was derived from a desmoplastic medulloblastoma and harbors a C242F p53 mutation^{13,14}.

Immortalized human benign meningeothelial meningioma cells (BMEN1)¹⁵ were used here as a model of normal meningeothelial cells that were obtained from the DSMZ animal cell culture collection (Braunschweig, Germany) and cultured in DMEM containing 20% FBS and 1% penicillin/streptomycin.

Fibroblastic human meningeal cells were obtained (cat #1400, ScienCell Research Lab, Carlsbad, CA) and cultured in Meningeal Cell Medium (MenCM, cat #1401, ScienCell Research Lab) supplemented with meningeal

cell growth supplement (MCGS, cat #1452, ScienCell Research Lab) and 2% FBS with 1% penicillin/streptomycin.

Tissue microarray immunohistochemistry

The children's oncology tissue microarray 300-30-P8146 was stained by Robert E. Brown using clinical protocol rIGF on the IntelliPATH FLX (Biocare Medical, Pacheco, California) system (Supplementary Fig. 1).

IC₅₀ studies

D425 cells were cultured in growth media, trypsinized, and then resuspended in either growth media with FBS or growth media without FBS. The cells were plated into a 384-well plate at 1200 cells per well in 30 μ L of media and incubated for 24 h. BMS-754807 was added to both the D425 cells in media with and without FBS using the Tecan300e. Cells were incubated for 72 h, and then CTG 2.0 (cat#PRG9242, Fisher Scientific, Hampton, NH) was added, rocked for 15 min, and imaged using a microplate reader (D300e, Tecan, Männedorf, Switzerland) (Supplementary Fig. 2).

Cell adhesion assays

BMEN1 cells were plated at ~60% confluence in appropriate media in uncoated ibidi micro-slide IV channels (cat#80666, ibidi, Grafeling, Germany) and allowed to establish for 24 h prior to experimentation. GFPsD425 cells were suspended in PBS at a cell density of 1.25e5 cells/mL. In some experiments, GFPsD425 cells were stained with 2 mM CellTracker Red (Thermo Fisher) for 45 min and then washed to remove excess dye. Prior to flow, the media is aspirated from the micro-slide well. GFPsD425 cell suspension was flowed through the micro-slide channel (cat#80666, ibidi) at 30 μ L/min using a syringe pump. A time-lapse series consisting of 180 red or green fluorescent images (1000 ms exposure time) over 4 min was collected per location, and two locations were tested per micro-slide channel. Images were processed in Fiji^{16,17} to quantify cell adherence over the course of each time lapse (see Supplementary Information for details of image processing).

To examine the effect of IGF1 stimulation on cell-cell adhesion, rhIGF1 (cat#CYT-216, Prospec, Rehovot, Israel) was added to the GFPsD425 suspension at a concentration of 10 ng/mL 15 min prior to experimentation. To examine the effect of the InsR/IGF1R small molecule inhibitor BMS-754807 on adhesion, BMS-754807 (cat#S1124, SelleckChem, Radnor, PA) was added to the GFPsD425 suspension at a concentration of 231.8 ng/mL 15 min prior to experimentation¹⁸. To examine the effect of IGF1 knockdown on adhesion, ON-TARGETplus SMARTpool IGF1R siRNA (cat#L-003012-00-0005, Dharmacon, Lafayette, CO) was added in combination with Lipofectamine® RNAi-MAX Reagent (cat#13778075, Thermo Fisher) to GFPsD425 culture in Opti-MEM® Medium (cat#A4124802, Thermo Fisher), per the manufacturer's instructions (Supplementary Fig. 3). Cells were incubated at 37 °C for 24 h prior to analysis.

BMS-754807 pharmacodynamic analysis in mice

BMS-754807 (cat#S1124, SelleckChem) was dissolved in a mixture of polyethylene glycol and water (PEG₄₀₀ 4:1 H₂O). Six 6–8-week-old SHO mice were administered 0 ($n = 1$), 12.5 ($n = 1$), 25 ($n = 1$), or 32.5 mg/kg ($n = 3$) BMS-754807 orally every 12 h for a total of 3 doses each. Mice were sacrificed 12 h following their final dose to assess steady-state IGF1R activity levels in tissue. IGF1R activity in tissue lysates was assessed by western blotting. All experiments were conducted in accordance with ethical guidelines and protocols and were approved by the Children's Cancer Therapy Development Institute IACUC protocol number 2017-003.

Immunoblotting

For western blot analysis of tissue cultures, plates of confluent cells were washed with PBS, scraped into 10 mL PBS, collected by centrifugation at 1200 rpm for 5 min, and lysed in radioimmunoprecipitation assay (RIPA) buffer (cat#89901, Thermo Fisher Scientific) with 3x Halt™ protease and phosphatase inhibitor (cat#78420, Thermo Scientific). Lysates were clarified by centrifugation at 800 \times g for 10 min. A bicinchoninic assay (BCA) was

performed on supernatants that were normalized for protein content, colored with the addition of bromophenol blue to 0.05%, reduced with the addition of DTT to 50 mM, and heated to 95 °C for 5 min. Eighty microgram of protein from each extract was electrophoresed in 10% polyacrylamide gels. After transfer to PVDF membranes, western blot analysis of IGF1R activity was performed using rabbit anti-phospho-IGF1R antibody (ab39398, Abcam) and rabbit anti-IGF1R antibody (ab39675, Abcam) as primary antibodies at a 1:1000 dilution. Goat anti-rabbit IgG (H+L) cross-adsorbed secondary antibody conjugated to Alexa Fluor 647 (115-606-146, Jackson ImmunoResearch Laboratories) was added to visualize bands using a Bio-Rad ChemiDoc MP Imaging System (Bio-Rad).

For mouse study immunoblotting, tissues were kept on ice following animal sacrifice, homogenized in RIPA buffer + 3x Halt™ (cat#78420, Thermo Scientific), and then centrifuged at 14,000 rpm for 10 min at 4 °C, after which the protein supernatant was collected. Following protein quantification by BCA, 80 µg of protein from each extract was electrophoresed in 10% polyacrylamide gels. Western blotting was performed with rabbit anti-phospho-IGF1R antibody, rabbit anti-IGF1R antibody, and mouse anti-β-actin antibody (A1978, Sigma-Aldrich) as primary antibodies at a 1:1000 dilution. Goat anti-rabbit IgG (H+L) cross-adsorbed secondary antibody conjugated to Alexa Fluor 647 was added to visualize bands using a Bio-Rad ChemiDoc MP Imaging System (Bio-Rad).

DNA and RNA sequencing

All relevant ethical regulations were followed, and informed consent was obtained from the patient's parent, and approval was obtained from the Institutional Review Board at Children's Cancer Therapy Development Institute (Advarra, protocol #cc-TDI-IRB-1), this consent and approval covers sequencing, in silico modeling, tissue staining, and clinical history. Tumor and matched normal exome sequencing data were analyzed for the presence of somatic point mutations, somatic functional/structural mutations, potential germline mutations, polynucleotide insertions/deletions, and gene copy number variations. Somatic mutations, variations, and indels were called using Genome Analysis Toolkit Version 4.0 with strict calling criterion (Tumor logarithm of odds [TLOD] scores above 10.0)¹⁹ with the GRCh38 human reference genome. Gene copy number variations were identified using SAMtools²⁰ and VarScan2²¹ quantified as the log ratio of tumor copy number divided by normal copy number. Regions with log ratio > 0.75 were called gained, and regions with log ratio < -0.75 were called lost. Genes overlapping gained or lost regions by at least 10% of the gene's genomic region were called gained or lost, respectively.

RNA sequencing data were analyzed for gene expression and gene fusion events. Transcriptome data were aligned to the STAR-derived²² human transcriptome from the GRCh38 human reference genome. Normalized gene expression was quantified using RSEM²³. Nontumor gene expression data were not provided; thus, region-specific (brain: cerebellum) gene expression data were accessed from the Genotype-Tissue Expression project to serve as a population normal and to identify underexpressed and overexpressed genes. Gene fusion events were identified using STAR-Fusion to identify transcriptome reads around the junction of fused genes²⁴.

Medulloblastoma subtype analysis

Genomics and transcriptomics data from the complete analysis set were mapped onto the features reported to constitute the 4 canonical medulloblastoma subtypes (WNT, SHH, Group 3, Group 4)²⁵. Given the lack of clear subtype membership, the omics data were further mapped on the genomic and transcriptomic data onto Subtypes I–VIII²⁵, which previous work identified as further subdivisions of Group 3 and Group 4 specifically, as shown in Fig. 1. The level of evidence support was determined by the presence or absence of the specific features as binary computations.

In silico trials for patient-specific computational fluid dynamics modeling of drug solute transport within the cerebrospinal fluid

We utilized the following computational fluid dynamics (CFD) method to solve for and define patient-specific drug exposure over the tumor surfaces

as a function of time after drug injection within the lateral ventricle and throughout the CSF system (Fig. 2). This method checked for numerical time-step and mesh independence, and verified experimentally in the context of intra-CSF solute transport by Khani et al.^{26–28}. Here, we provide a brief description of the key methods and additional details relevant to the patient-specific simulation and injection device.

Complete details on the imaging processing steps used for numerical model geometric and flow boundary conditions are described by Sass et al.²⁹ and Seiner et al.³⁰. In brief, to define the lesion location and geometry, a series of MR images were collected with full brain coverage at 3 T (GE, Discovery MR750, Software version DV25.0 R01 1451.a, Boston, MA). Axial DWI was collected with 2 mm slice thickness and spacing (TR 12977, TE 56.8, averages = 2, FA 90, 0.859 mm isotropic in-plane pixel spacing). Axial 3D FLAIR images were collected with 1 mm slice thickness and spacing (TR 5650, TE 128.7, Inversion time 1607, 0.5 isotropic in-plane pixel spacing). Axial 3D BRAVO images were collected with 1 mm slice thickness and spacing (TR 11.1, TE 4.66, FA 15, 0.5 isotropic in-plane pixel spacing). These images were utilized to measure the location and size of two tumor lesions, one located near the cranial base posterior to the brainstem occupying space within the upper cervical spine and having an approximate diameter of 25 mm and another lesion located within the lateral ventricular horn with an approximate diameter of 4 mm (Fig. 2). In addition, the patient had a ventriculoperitoneal shunt implanted in the left lateral ventricular horn with an inner diameter of 1.4 mm.

The 3D tumors and shunt geometry were manually added to a previously published pharmacokinetic model^{26,30} of the CSF system for subsequent simulation. In brief, the previously published pharmacokinetic model of the CSF system was defined based on high-resolution T2-weighted images with full neuraxial coverage. Images were manually segmented to define the CSF geometry around the spinal cord and brain (extra-axial CSF) and within the ventricles of the brain (lateral ventricles, 3rd ventricle, and 4th ventricle). Spinal cord nerve rootlets with realistic radicular line, descending angle, and diameters, and filum terminale with “horse tail” fibers were added to the spinal cord based on visual inspection of the MR images and review of the anatomic literature²⁹.

An in silico CFD simulation was performed to estimate the average drug exposure over the tumor surface following an 85 mg injection of BMS-754807 drug (461.5 g/mol) via the ventricular catheter that was infused at a rate of 0.00139 mL/min over a period of 24 h for a total infusion volume of 2.0 mL. These injection parameters were based on reference¹⁸. The CFD model included subject-specific oscillatory CSF flow within the ventricles and aqueduct of Sylvius and a 0.4 mL/min CSF production rate originating from the choroid plexus within the lateral ventricles. Based on previous phase-contrast MRI measurements of CSF flow by Lagana et al.³¹ and our research team³², the CSF stroke volume within the aqueduct of Sylvius was set to 1/36 of the spinal subarachnoid space at the C2/C3 vertebral level, with 1/2 arising from CSF pulsations within each lateral ventricle. CSF flow oscillations were also imposed along the spinal subarachnoid space and around the cortical subarachnoid space with a stroke volume of 1 mL and 66 beats/min, similar to our previous research³⁰.

Using the above boundary conditions, a multi-phase CFD simulation was conducted for a duration of 8 h post-drug infusion utilizing the ANSYS FLUENT finite volume solver environment (Canonsburg, Pa, Version 19). This involved solving for the oscillatory CSF velocity field based on the continuity equation (Eq. 1) and Navier–Stokes equation (Eq. 2) with a gravity term, where ρ is the density, μ is the fluid viscosity, g is acceleration due to gravity, $u^-(x^-, t)$ is the velocity vector and p is the pressure field³³.

$$\bar{\nabla} \cdot [\rho \bar{u}(x^-, t)] = 0 \quad (1)$$

$$\rho \frac{\partial \bar{u}}{\partial t} + \rho \bar{u} \cdot \bar{\nabla} \bar{u} = -\bar{\nabla} p + \bar{\nabla} \cdot \mu \bar{\nabla} \bar{u} + \rho \bar{g} \quad (2)$$

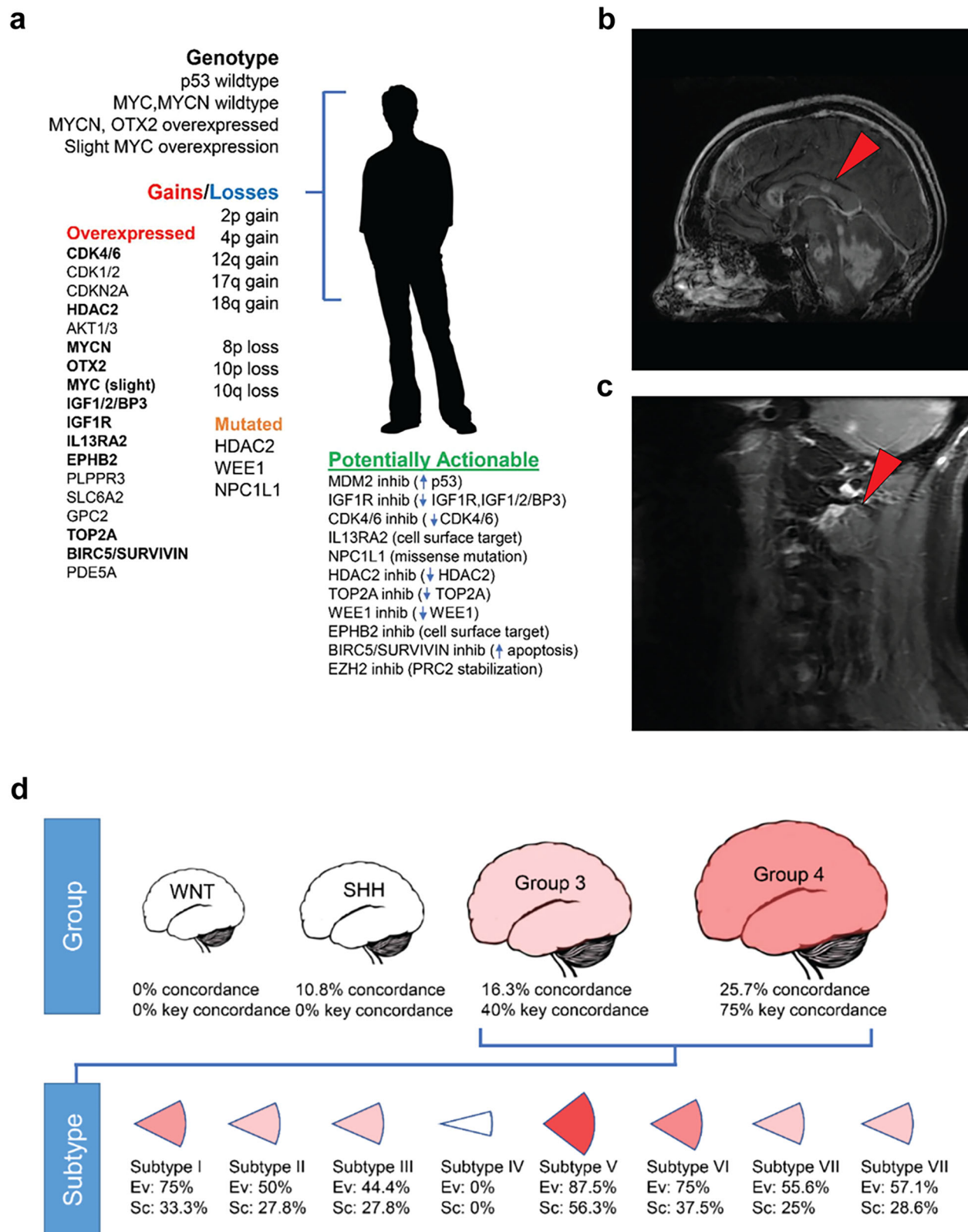


Fig. 1 | Patient-specific data. a Patient case genetics summary (see Supplementary File 1 for details). **b** Patient's relapse MRI of intraventricular metastasis (4 mm). **c** C1 metastasis (25 mm). Multiple tumors are visible, but the intraventricular and C1

metastasis tumors were chosen for computational analysis. **d** Analysis of genetic mutations, copy number, and gene expression suggests medulloblastoma molecular Subtype V.

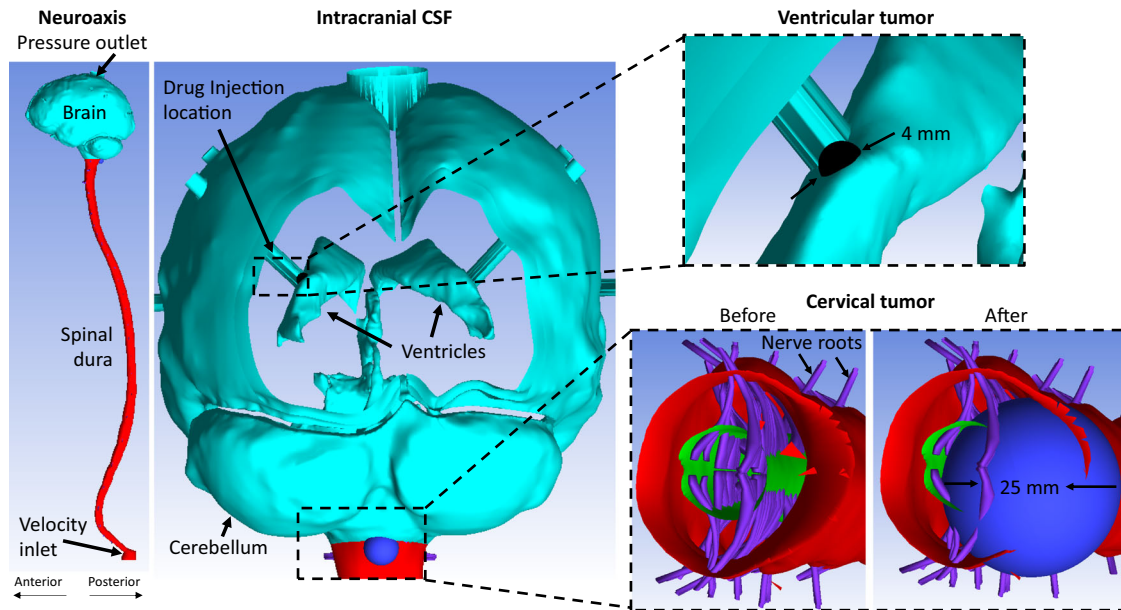


Fig. 2 | 3D computational fluid dynamics model geometry used to simulate CSF system-wide drug solute transport during drug injection in the lateral ventricular horn. The red section of the model indicates the spinal subarachnoid space, including spinal cord nerve rootlets (see detail). The light blue section indicates the cranial subarachnoid space and ventricular cisterns (lateral ventricles, third

ventricle, and 4th ventricle). A 4 mm ventricular tumor was located on the superior aspect of the left ventricular horn. A 25 mm cervical tumor was located posterior to the C1 vertebral level, occupying ~50% of the total subarachnoid space cross-sectional area at that location.

The drug dispersion was solved using the ANSYS mixture multi-phase fluid model with the tracer volume fraction given by Eq. 3:

$$\frac{\partial}{\partial t}(\alpha_k \rho_k) + \nabla \cdot (\alpha_k \rho_k \vec{v}_m) = -\nabla \cdot (\alpha_k \rho_k \vec{v}_{dr,k}) \quad (3)$$

With q as the bulk fluid phase, ρ_k and α_k as the phase density and volume fraction of phase k , $\vec{v}_m = \frac{\sum_{k=1}^n \alpha_k \rho_k \vec{u}_k}{\rho_m}$ is the mass-averaged velocity, ρ_m is the mixture density, and $\vec{v}_{dr,k}$ is the drift velocity for phase k . The drift velocity was specified to be zero, with a slip velocity between phase k and the bulk fluid assumed to be zero.

The model mesh size was ~2 million tetrahedral elements with refinement near the injection area and around spinal cord nerve rootlets and other detailed anatomical structures. Based on our prior numerical independence studies, the model convergence criteria were set to 1e-06 for velocity, continuity, momentum, and phase volume fraction with a maximum of 100 iterations per time-step. Intrathecal drug molecular diffusion has previously been found to be small³⁴ and therefore was not included in the model³⁵. Time-step size was set to 10 ms with a maximum mesh element size of 0.5 mm. Drug buffer properties were assumed to be identical to the CSF with a density of 998.3 kg/m³ and viscosity of 0.89 mPa-s³⁶.

Tumor drug exposure was quantified in terms of the average drug concentration within the CSF over the tumor surface with respect to time. This information was then utilized as an input boundary condition for the in vitro drug exposure experiments described below. To help visualize the overall drug dispersion, we computed the spatial-temporal distribution of tracer concentration for 3 mm slice intervals along the entire neuroaxis based on Eq. 4:

$$\alpha(z) = \frac{\sum_{\text{slice}} |\alpha_k(z)| V(z)}{\sum_{\text{slice}} V(z)} \quad (4)$$

where $\alpha(z)$ is the axial distribution and V is the cell volume computed based on the summation of all cells within each 3 mm slice.

Microfluidics studies

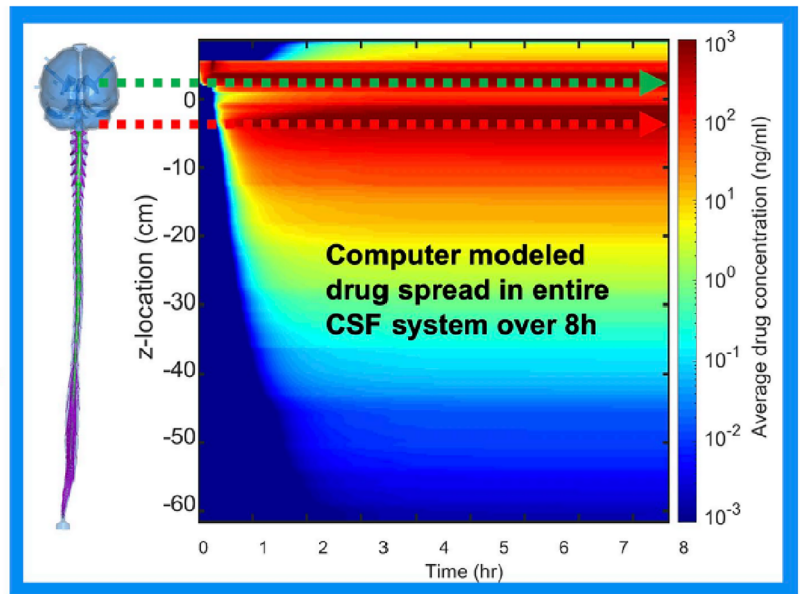
BMEN1 cells were suspended in DMEM containing 20% FBS and 1% penicillin/streptomycin at a cell density of 4e6 cells/mL. At this cell density, 10 μ L of suspended BMEN1 cells was plated inside the channels of an uncoated ibidi micro-slide VI 0.1 (cat#80666, ibidi) and incubated for 5 min at 37 °C. Once removed from the incubator, 50 μ L of media was dispensed into each well and then incubated for 24 h at 37 °C. GFPsD425 cells were suspended in DMEM containing 20% FBS and 1% penicillin/streptomycin at a cell density of 4e6 cells/mL. Then, 50 μ L of media from each well was aspirated, and 10 μ L of suspended GFPsD425 cells were plated atop the BMEN1 cells inside the channels of the ibidi micro-slide VI 0.1 (cat#80666, ibidi). Immediately after dispensing the GFPsD425 cells, 50 μ L of media was dispensed into each well. The ibidi micro-slide VI 0.1 (cat#80666, ibidi) was incubated for 72 h at 37 °C to allow for the adhesion of GFPsD425 cells to BMEN1 cells.

To prevent bubble formation, two 40 mL containers of DMEM containing 20% FBS with 1% penicillin/streptomycin were placed in a vacuum chamber for 15 min at a pressure of 30 inches Hg. BMS-754807 (molecular weight 461 gm/mol) (cat#S1124, SelleckChem) was diluted with DMSO to a concentration of 13.2 ng/mL based on the median drug concentration after 8 h (Fig. 3). Two 30 mL syringes were loaded with the drug and control. An Inline Bubble Trap, 300 μ L, was attached to an ibidi tube adapter connected to the wells of the ibidi micro-slide (cat#80666, ibidi). The flow rate was obtained from the manufacturer's Application Note 11: Shear Stress and Shear Rates (cat#80666, Application Note 11, ibidi) using the average wall shear stress of 0.0514 Pa on the surface of the spinal cord and brain³⁷. Drug and media flowed through the micro-slide channel at 0.4 mL/h (given for cat#80666, Application Note 11, ibidi) using a syringe pump. Green fluorescent images were captured with 4 \times 4 tiles in Z-stacks of three 10 μ m apart every 30 min for 72 h on a Zeiss LSM700 confocal microscope (magnification level: 200 \times) as shown in Fig. 4. Images were analyzed using

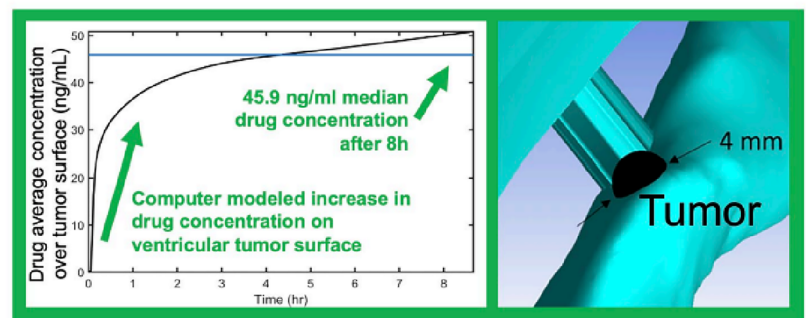
Fig. 3 | CSF-system-wide computational pharmacokinetics for intraventricular drug delivery.

a Model results for a single 17 mcg dose of BMS875807 in a 2 mL bolus injected into the lateral ventricle, followed over 8 h. **b, c** Average drug concentration of 45.9 ng/mL and 13.2 ng/mL, over the ventricular and C1 tumor surface, respectively, computed over an 8-h time period. For reference, the EC₅₀ of this drug for its target IGF1R IC₅₀ 1.8 nM (13.8 ng/mL), which appears yellow-red. For reference, the clinical C_{max} (232 ng/mL), which appears red-dark red in (a).

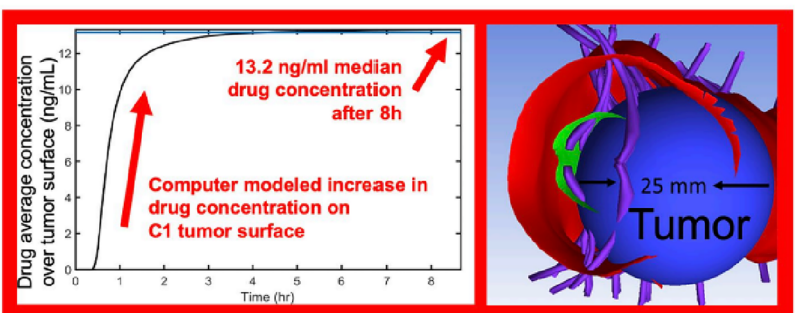
a



b



c



Fiji for cell area coverage of the GFPsD425 cells (see Supplementary Information for details of image processing).

Statistics and reproducibility

For Fig. 5 and Supplementary Fig. 4, *p* values were calculated in GraphPad Prism software (v.10.1.0) using an unpaired two-tailed *t*-test, and the estimated effect size is determined by Hedges' *G* with small sample size

correction. For Fig. 4 the *p* values were calculated using a two-way ANOVA in GraphPad Prism. The *n* values for each figure are listed with each figure or caption.

Reporting summary

Further information on research design is available in the Nature Portfolio Reporting Summary linked to this article.

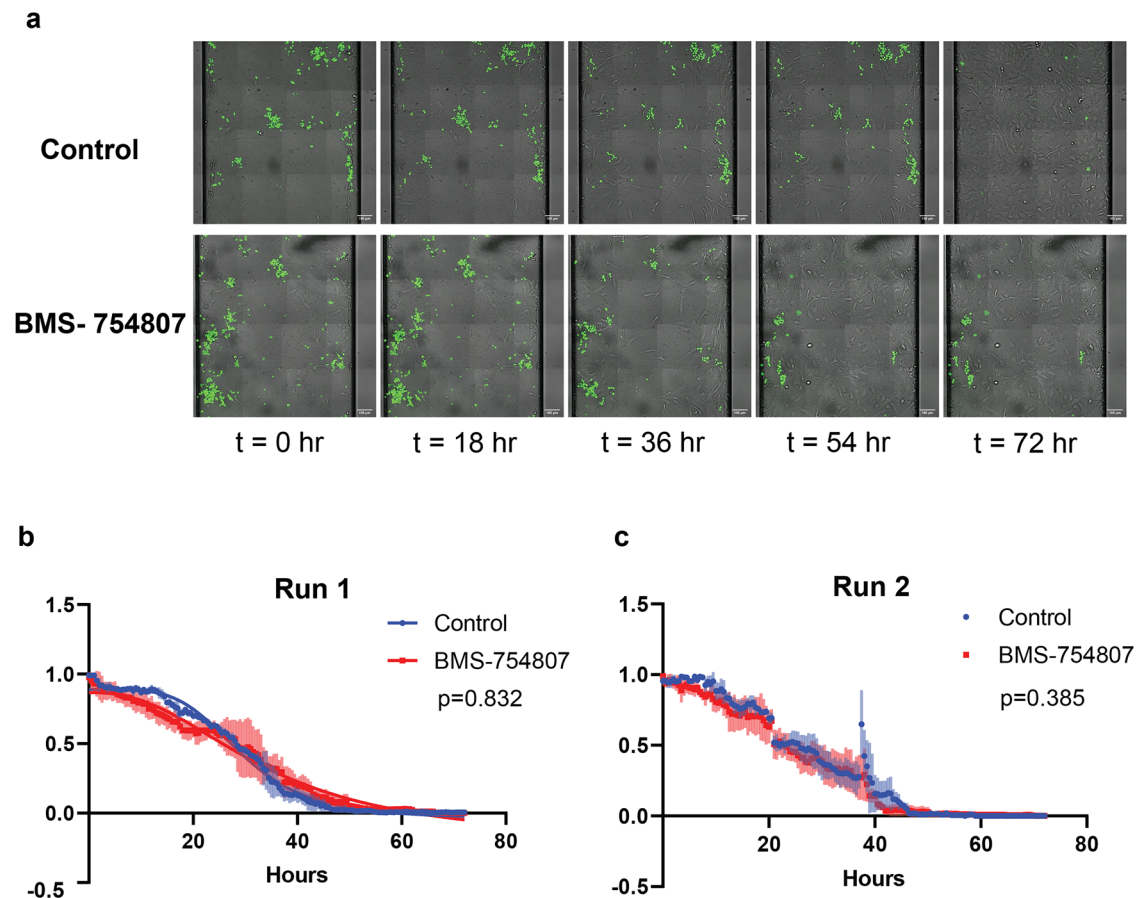


Fig. 4 | Time series images for patient-specific drug exposures with no change in viability of established metastases. **a** Microfluidics channel slide time-lapse imaging of green fluorescent GFP+ D425 medulloblastoma cells (GFPsD425) co-cultured atop unlabeled BMEN meningeothelial cells while exposed to a continual flow of control media (top row) or BMS-754807 at 13.2 ng/mL (bottom row) for 72 h. GFPsD425 cells were allowed 72 h to adhere to the BMEN1 cells in the channels under static (non-flow) conditions before drug exposure. The flow rate within the

channels was 0.04 mL/h to model the average shear stress of 0.0514 Pa experienced on the brain and spinal cord from the CSF³⁷. **b, c** Two independent runs of viable tumor cell mass over time. Normalized GFPsD425 cell area percentage in the field of view exposed in the microfluidic channel to drug-free media or BMS-754807 under shear stress and drug exposure stated above, with areas imaged being $n = 3$ for run 1 and $n = 2$ for control and $n = 3$ for BMS-754807 for run 2, with the error bars being the standard deviation.

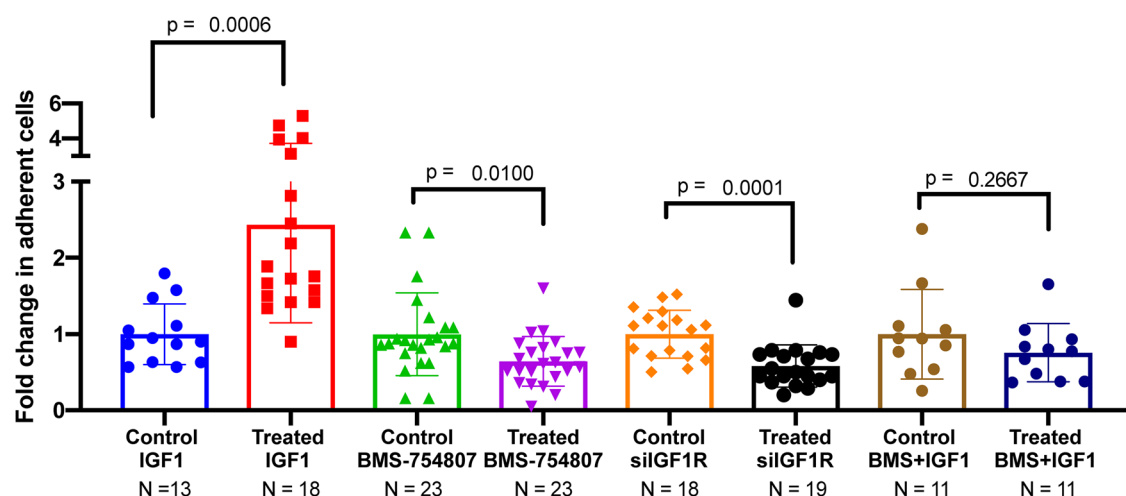


Fig. 5 | BMS-754807 reduction of initial medulloblastoma cell adhesion to meningeal cells in an in vitro flow model. GFP-tagged or CellTracker-stained D425 cells flowed over meningeal cells for 5 min, and the proportion of adhered cells was recorded. Each treatment group was compared against its own control group. For IGF1, BMS-754807 experiments, control cells were treated with vehicle. For this

siIGF1R experiment, the Ibicontrol was siScramble-treated cells. For BMS + IGF1 experiments, control cells were treated with IGF1, and the experimental condition was treatment with BMS-754807 for 5 min prior to a 15-min treatment with IGF1. The flow condition was 30 μ L/min in ibidi micro-slide IV channels, giving a shear stress of 0.00284 Pa. The error bars are the standard deviation for each column.

Results

Clinical history of patient-derived primary cell culture

A 12-year-old male patient was initially diagnosed with Group 4 medulloblastoma and underwent gross total resection for a solitary primary tumor and chemoradiation 1 month later. The patient then remained disease-free for 28 months before developing a 4 mm lesion along the left lateral ventricle and a 7 mm nodule within the spinal cord at level T12, which were subsequently resected. The patient then underwent high-dose chemotherapy followed by stem cell transplantation and dendritic therapy. Three months later, the patient developed a stable small hemorrhage in the left frontal horn, which corresponded to the previous tumor site. No evidence of recurrent or metastatic disease in the brain was observed between 36 months and 45 months post-initial diagnosis. Two months later, disease recurrence was suspected due to the interval development of a nodule along the ependymal margin of the frontal horn of the left lateral ventricle near the genu of the corpus callosum. Three months later and 51 months post-initial diagnosis, recurrence at the same point of ventricle resection was observed and subsequently irradiated by CyberKnife. Three months later, two new lesions in the atria and temporal horn of the left lateral ventricle were discovered and treated with one dose of intrathecal measles virus. Concurrent with virus therapy, two small new lesions were detected on MRI within the right aspect of the pons. The patient then began metronomic chemotherapy, which was stopped after 3 weeks due to thrombocytopenia and lymphopenia. Fifty-six months from initial diagnosis, an increase was observed in the size of the right brainstem lesions with no substantial changes in lesions along the ependymal surface of the left lateral ventricle. Two months later, the patient became symptomatic with an acute onset of numbness in the right upper extremity, face and leg, slurring words, and balance issues along with two new lesions in the brainstem and left lateral ventricle, and increasing medulloblastoma nodular size. The patient then started localized radiation and interval steroid treatment with some efficacy in stabilizing the disease. Disease progression 3 months later, 61 months from initial diagnosis, with new extension into the right brachium pontis, right superior cerebellar peduncle, and right superior cerebellum. The patient started treatment with anti-CD47 therapy but was abandoned due to ongoing thrombocytopenia. Sixty-three months from the initial diagnosis, two new lesions appeared on the right aspect of the corpus callosum and frontal horn of the right lateral ventricle, which were irradiated by CyberKnife, followed by two infusions of a PD-1 inhibitor. One month later, new lesions appeared within the medial left cerebellar hemisphere, dorsal subarachnoid space from T5 to T10, and within the spinal cord at level T12, with increasing growth of lesions at the genu of the corpus callosum. Continued disease progression at 66 months from diagnosis of intracranial medulloblastoma with an increase in the size and number of lesions within the brain parenchyma, subependymal surfaces of the lateral ventricles and fourth ventricle, brainstem, cerebellum, medulla, and C1-2 level of the cervical spinal cord. The patient then received IL-7 therapy. Shortly thereafter, the patient passed away from complications of CNS disease. Tumor tissue from primary cell culture development was collected at autopsy.

Molecular subtyping of the patient's medulloblastoma and matching to a cell line (D425)

Medulloblastoma subtype analysis was performed using the genomics and transcription data provided in Supplementary File 1—Tumor Genetics Report. The patient's tumor exhibited moderate concordance with Group 3/ Group 4 medulloblastoma subtype V (*TP53* wild-type, *MYC/MYC* wild-type, *MYCN* and *OTX2* overexpression, partial *MYC* overexpression, *IGF1R* overexpression). Group 3/4 medulloblastoma cell line D425 was chosen as a representative of the patient's tumor due to *MYC* amplification, *IGF1R* overexpression, no *MYCN* amplification, and *TP53* was normal.

Prevalence of *IGF1R* in medulloblastoma biopsies

Using a tissue microarray, protein expression was assessed by immunohistochemistry. Overall, 74.7% of samples had some level of *IGF1R* expression (Table 1, Supplementary Fig. 1).

Table 1 | Scoring of tissue microarray immunohistochemistry for *IGF1R*

Score	Sample count
Total number of tumor samples	99
Number of usable samples	79
Samples with score = 0	20 (25.3%)
Samples with score = 0/1	15 (19.0%)
Samples with score = 1	22 (27.8%)
Samples with score = 1/2	1 (1.3%)
Samples with score = 2	10 (12.7%)
Samples with score = 2/3	1 (1.3%)
Samples with score = 3	8 (10.1%)
Samples with score = 4	2 (2.5%)

A tissue microarray was performed, and each tumor sample was given a score for the level of expression: 0 for no expression, 1 for faint expression, 2 for detectable fair expression, 3 for the same level of intensity as normal cerebellum, and 4 for higher intensity than normal cerebellum.

Representative tissues from scores 0, 1, 2, 3, and 4 were chosen for the expression of *IGF1R* and displayed in Supplementary Fig. 1.

Patient-specific CFD analysis of tumors drug exposure following dosing

Based on the patient-specific CFD simulations mapping tumor locations and volume to an idealized finite-element CSF flow model, the average drug concentration within the CSF was determined along the entire neuroaxis for a period of 8 h following ventricular dosing (Fig. 3a and Video in Supplementary Data). Within ~15 min post-ventricular injection, the drug dispersed from the lateral ventricles through the foramen of Monro, into the 3rd ventricle and out to the cisterna magna and basal cisterns of the brain via the foramen of Magendie and Luschka. Subsequently, the drug dispersed around the cortical subarachnoid space and spinal cord. Average cross-sectional drug concentrations decreased substantially along the spine by greater than 6 logs compared to the injection site. Additionally, drug concentrations decreased rapidly around the cortical subarachnoid space, with the lowest levels near the parietal and occipital lobes.

The average drug concentration over the ventricular tumor (Fig. 3b) increased to ~35 ng/mL within the first hour following infusion commencement. After 8 h of continuous infusion, the median drug concentration was 45.9 ng/mL. The average drug concentration over the C1 tumor (Fig. 3c) increased to ~11 ng/mL within the first hour and leveled off asymptotically at a median drug concentration of 13.2 ng/mL after 8 h of infusion.

Microfluidic studies revealed no drug effect at the modeled concentration for physiological concentrations

Using time-lapse microfluidics, medulloblastoma D425 cells were co-cultured atop leptomeningeal cells and exposed to the *IGF1R* inhibitor drug under physiological CSF flow conditions to model intrathecal and intra-ventricular drug administration to established leptomeningeal metastasis. When conducting microfluidic channel slide experiments at physiological concentrations according to Fig. 2 with a shear stress equal to 0.0514 Pa, the percentage of established tumor cells on leptomeningeal cells was measured over a 72-h period. The BMS-754807 and control channel slides had continuous detachment of tumor cells, decreasing the coverage percentage. No significant difference was found between the control and BMS-754807, with both D425 cell cultures decreasing in surface coverage for the experiment.

Generalized proof-of-concept for *IGF1R* inhibitor BMS-754807 to reduce attachment under flow conditions

The overexpression of the *IGF1R* protein in medulloblastoma cells was targeted as a potential promoter of leptomeningeal metastasis. A low shear stress of 0.00284 Pa was used to allow for possible attachment of the D425 cells as they flowed across cultured BMEN1 cells in a microfluidic channel slide. The D425 cells were treated with *IGF1* and BMS-754807 as the D425

cells passed through the channel slide. These studies suggested that IGF1 binding to IGF1R promotes metastasis-like attachment of medulloblastoma cells that overexpress IGF1R⁵. The channel slide experiments shown in Fig. 5 show a statistically significant adhesion increase in D425 cells when treated with IGF1 ($p = 0.0006$, estimated effect size 1.37). A statistically significant decrease in D425 adhesion was observed when treated with BMS-754807 ($p = 0.0100$, estimated effect size 0.78) and when *IGF1* is silenced ($p = 0.0001$, estimated effect size 1.38).

Confirmation that BMS-754807 partially crosses the blood–brain barrier

Crossing the blood–brain barrier will increase the concentration of the drug at the targeted site. To confirm partial crossing of BMS-754807, mice were dosed with the drug orally, and their cerebellum tissue was analyzed by western blot for IGF1R activity. The phosphorylation of IGF1R indicates binding of IGF1 or IGF2 to the protein receptor. Measuring the ratio of phospho-IGF1R to IGF1R shows the inhibition of IGF1R in the cerebellum. A statistically significant decrease of phospho-IGF1R from BMS-754807, having crossed the blood–brain barrier, was observed ($p = 0.0017$, estimated effect size 3.8) (Supplementary Fig. 4).

Discussion

For medulloblastoma, the blood–brain barrier prevents many therapeutic agents from reaching the tumor. Delivering therapy via intraventricular CSF infusion bypasses the blood–brain barrier and can directly address leptomeningeal metastasis. In our patient-specific example, *IGF1R* was an overexpressed gene, and our experimental results revealed that inhibition of IGF1R can decrease cell adhesion. Using models from patient MRI, channel slide experiments were conducted at physiological concentrations and stress with D425 cells adhered to BMEN cells to test inhibition of already existing metastasis. Wall shear stress could only match the average shear stress and not follow the constant changes in the cardiac cycle. No difference existed between the control and BMS-754807 in the microfluidic slide experiments for already established metastases.

The major finding of this study is that patient-specific 3D CSF modeling can be applied to predict the drug exposure at each tumor surface following drug injection within the lateral ventricle. These physiologically based pharmacokinetic simulations allowed the integration of transport phenomena introduced from both complex geometry and flow dynamics that underlie the movement of solutes through the CSF system. The strength of this modeling approach allowed detailed implementation of anatomic and physiological boundary conditions that integrated specific tumor sizes and locations. These boundary conditions have been found to alter drug exposure to a great degree^{26,30,33}. While for the present retrospective study, the exact CSF flow waveform and geometry of the patient's entire CSF system were not obtained by MRI, such data could be collected prospectively for future studies. It is expected that patient-specific CSF flow and geometric alterations could have a substantial impact on drug solute transport characteristics. For example, for patients with obstructive hydrocephalus, focal spinal stenosis, scoliosis, and/or microcephaly, drug transport would likely be different. Studies in the literature have shown CSF dynamics alterations in CNS disease states^{38–40}, and therefore, these alterations would impact solute transport. Thus, the simulations presented are predictive but could be improved by patient-specific collection of exact CSF flow waveforms and system geometry. For the present study, we were able to apply the model and determine that an 85 mg drug injection in 2 mL over a 24-h duration resulted in an average drug–tumor exposure ranging from ~10 to 50 ng/mL, depending on tumor location at C1 or ventricular horn, respectively.

Additional parametric computational studies could be performed to quantify the potential range of drug exposures given patient population variability in CSF geometry and flow, but were outside the scope of this research. For example, the computational model assumed a CSF production rate of 0.4 mL/min and aqueductal stroke volume of 0.028 mL (1/36 of spinal subarachnoid space). The specific patient may have had a greater or smaller CSF production rate and/or stroke volume. The CSF geometry of the

ventricles was assumed to be impacted only by an idealized tumor lesion. In actuality, the patient had complex anatomic alterations coinciding with the disease state. These alterations could be integrated utilizing detailed patient-specific models. The presented model was performed with rigid walls representing the dura and CNS tissues and therefore neglected craniospinal compliance along the neuroaxis. A compliant model may alter model predictions and could be implemented in future research. Also, previous studies have shown that ependymal cilia lining the ventricular wall could also impact near-wall CSF dynamics⁴¹.

We note that even 8 h following drug injection, a large portion of the injected drug volume remained in the ventricles, a factor previously reported by our research team²⁶. Residual drug in the ventricles could be advantageous if drug exposure is desired within the ventricles. However, if drug exposure is desired in the subarachnoid space surrounding the brain and spinal cord, injection protocols could be optimized to achieve that objective, for example, by altering the drug density, injection rate, volume, patient orientation, and injection device. Concerning drug density, this would be a factor of the infusion buffer formulation and drug molecule properties. In the present study, we assumed the drug buffer to be identical to water at body temperature. Drug characterization could be performed to specify exact fluidic properties and integrated into the model.

Finally, this study has several limitations that should be addressed in future studies. These caveats include understanding the difference between bound and free drugs in the serum, cerebrospinal fluid, and cell culture media. Biological factors that require nuanced consideration include tumor cell heterogeneity (i.e., that cell lines are imperfect homogeneous tumor cell populations) and patient-to-patient variability in drug metabolism and blood–brain barrier drug transport and efflux. While the tumor locations and sizes were taken from an actual clinical case's MRI scans, an area of future study for our group will be to build deformable CNS models that could be used for larger tumors. The digital model in this study was formulated based on patient-specific CSF system geometry and flow. Different patients and their associated disease phenotypes are expected to impact model results. For example, if a particular patient had reduced cerebroventricular volume, it is expected that the drug buffer injection volume would potentially disperse out of the ventricles with altered drug kinetics, leading to changes in drug target interactions with the tumor surfaces. The digital model results focused on the injection of a neutrally buoyant drug buffer with identical density and viscosity to CSF at body temperature. Alteration of drug buffer properties can impact model results and could be parametrically analyzed in combination with other injection parameters such as volume and rate, along with physiological inputs such as cardiac rate, respiratory rate, and other factors, but was outside the scope of the present study. Nonetheless, the current study creates proof-of-concept for generalized computational predictive modeling of CNS drug exposures over time.

Data availability

Source data (numerical data) for Figs. 4 and 5, as well as Supplementary Figs. 2 and 4 are located in the Supplementary Data File. Sequencing data were deposited with the European Genome-phenotype Archive under the deposit number EGAD50000000384.

Code availability

Instruction for the code used to analyze the microfluidic experiments is located in the Supplementary Information.

Received: 22 April 2024; Accepted: 16 May 2025;

Published online: 28 May 2025

References

- Partap, S. et al. Medulloblastoma incidence has not changed over time: a CBTRUS study. *J. Pediatr. Hematol. Oncol.* **31**, 970–971 (2009).

2. Fruhwald, M. C. & Plass, C. Metastatic medulloblastoma—therapeutic success through molecular target identification?. *Pharmacogenomics J.* **2**, 7–10 (2002).
3. Packer, R. J. et al. Medulloblastoma: clinical and biologic aspects. *Neuro Oncol.* **1**, 232–250 (1999).
4. Geyer, J. R. et al. Multiagent chemotherapy and deferred radiotherapy in infants with malignant brain tumors: a report from the Children's Cancer Group. *J. Clin. Oncol.* **23**, 7621–7631 (2005).
5. Moxon-Emre, I. et al. Impact of craniospinal dose, boost volume, and neurologic complications on intellectual outcome in patients with medulloblastoma. *J. Clin. Oncol.* **32**, 1760–1768 (2014).
6. Taylor, M. D. et al. Molecular subgroups of medulloblastoma: the current consensus. *Acta Neuropathol.* **123**, 465–472 (2012).
7. Kortmann, R. D. et al. Postoperative neoadjuvant chemotherapy before radiotherapy as compared to immediate radiotherapy followed by maintenance chemotherapy in the treatment of medulloblastoma in childhood: results of the German prospective randomized trial HIT '91. *Int. J. Radiat. Oncol. Biol. Phys.* **46**, 269–279 (2000).
8. Ramaswamy, V. et al. Risk stratification of childhood medulloblastoma in the molecular era: the current consensus. *Acta Neuropathol.* **131**, 821–831 (2016).
9. Svalina, M. N. et al. IGF1R as a key target in high risk, metastatic medulloblastoma. *Sci. Rep.* **6**, 27012 (2016).
10. Hakuno, F. & Takahashi, S. I. IGF1 receptor signaling pathways. *J. Mol. Endocrinol.* **61**, T69–T86 (2018).
11. He, X. M. et al. Differentiation characteristics of newly established medulloblastoma cell lines (D384 Med, D425 Med, and D458 Med) and their transplantable xenografts. *Lab Invest.* **64**, 833–843 (1991).
12. Friedman, H. S. et al. Phenotypic and genotypic analysis of a human medulloblastoma cell line and transplantable xenograft (D341 Med) demonstrating amplification of c-myc. *Am. J. Pathol.* **130**, 472–484 (1988).
13. Jacobsen, P. F., Jenkyn, D. J. & Papadimitriou, J. M. Establishment of a human medulloblastoma cell line and its heterotransplantation into nude mice. *J. Neuropathol. Exp. Neurol.* **44**, 472–485 (1985).
14. Raffel, C. et al. Absence of p53 mutations in childhood central nervous system primitive neuroectodermal tumors. *Neurosurgery* **33**, 301–305 (1993).
15. Puttmann, S. et al. Establishment of a benign meningioma cell line by hTERT-mediated immortalization. *Lab Invest.* **85**, 1163–1171 (2005).
16. Rueden, C. T. et al. ImageJ2: ImageJ for the next generation of scientific image data. *BMC Bioinform.* **18**, 529 (2017).
17. Schindelin, J. et al. Fiji: an open-source platform for biological-image analysis. *Nat. Methods* **9**, 676 (2012).
18. Clemens, P. L. et al. Abstract A101: BMS-754807, an oral dual IGF-1R/IR inhibitor: first-in-human single-dose study of safety, tolerability, pharmacokinetics, and pharmacodynamics in healthy subjects. *Mol. Cancer Ther.* **8**, A101–A101 (2009).
19. Geraldine, A. & Van der Auwera, B. D. O. C. *Genomics in the Cloud: Using Docker, GATK, and WDL in Terra* 1st edn (O'Reilly Media, Inc., 2020).
20. Li, H. et al. The Sequence Alignment/Map format and SAMtools. *Bioinformatics* **25**, 2078–2079 (2009).
21. Koboldt, D. C. et al. VarScan 2: somatic mutation and copy number alteration discovery in cancer by exome sequencing. *Genome Res.* **22**, 568–576 (2012).
22. Dobin, A. et al. STAR: ultrafast universal RNA-seq aligner. *Bioinformatics* **29**, 15–21 (2013).
23. Li, B. & Dewey, C. N. RSEM: accurate transcript quantification from RNA-Seq data with or without a reference genome. *BMC Bioinform.* **12**, 323 (2011).
24. Haas, B. J. et al. Accuracy assessment of fusion transcript detection via read-mapping and de novo fusion transcript assembly-based methods. *Genome Biol.* **20**, 213 (2019).
25. Northcott, P. A. et al. The whole-genome landscape of medulloblastoma subtypes. *Nature* **547**, 311 (2017).
26. Khani, M. et al. Human in silico trials for parametric computational fluid dynamics investigation of cerebrospinal fluid drug delivery: impact of injection location, injection protocol, and physiology. *Fluids Barriers CNS* **19**, 8 (2022).
27. Khani, M. et al. In vitro and numerical simulation of blood removal from cerebrospinal fluid: comparison of lumbar drain to Neurapheresis therapy. *Fluids Barriers CNS* **17**, 23 (2020).
28. Khani, M. et al. Anthropomorphic model of intrathecal cerebrospinal fluid dynamics within the spinal subarachnoid space: spinal cord nerve roots increase steady-streaming. *J. Biomech. Eng.* **140**, 0810121–08101215 (2018).
29. Sass, L. R. et al. A 3D subject-specific model of the spinal subarachnoid space with anatomically realistic ventral and dorsal spinal cord nerve rootlets. *Fluids Barriers CNS* **14**, 36 (2017).
30. Seiner, A. et al. Investigation of human intrathecal solute transport dynamics using a novel in vitro cerebrospinal fluid system analog. *Front. Neuroimaging* **1**, 879098 (2022).
31. Laganà, M. M. et al. Intracranial volumetric changes govern cerebrospinal fluid flow in the Aqueduct of Sylvius in healthy adults. *Biomed. Signal Process. Control* **36**, 84–92 (2017).
32. Bapuraj, J. R. et al. Cerebrospinal fluid velocity amplitudes within the cerebral aqueduct in healthy children and patients with Chiari I malformation. *J. Magn. Reson. Imaging* **44**, 463–470 (2016).
33. Khani, M. et al. Impact of neurapheresis system on intrathecal cerebrospinal fluid dynamics: a computational fluid dynamics study. *J. Biomech. Eng.* **142**, 0210061–0210069 (2020).
34. Tangen, K. et al. Clearance of subarachnoid hemorrhage from the cerebrospinal fluid in computational and in vitro models. *Ann. Biomed. Eng.* **44**, 3478–3494 (2016).
35. Kurtcuoglu, V. et al. Mixing and modes of mass transfer in the third cerebral ventricle: a computational analysis. *J. Biomech. Eng.* **129**, 695–702 (2007).
36. Bloomfield, I. G., Johnston, I. H. & Bilston, L. E. Effects of proteins, blood cells and glucose on the viscosity of cerebrospinal fluid. *Pediatr. Neurosurg.* **28**, 246–251 (1998).
37. Pahlavian, S. H. et al. Neural tissue motion impacts cerebrospinal fluid dynamics at the cervical medullary junction: a patient-specific moving-boundary computational model. *Ann. Biomed. Eng.* **43**, 2911–2923 (2015).
38. Sass, L. R. et al. Non-invasive MRI quantification of cerebrospinal fluid dynamics in amyotrophic lateral sclerosis patients. *Fluids Barriers CNS* **17**, 4 (2020).
39. Baledent, O. et al. Relationship between cerebrospinal fluid and blood dynamics in healthy volunteers and patients with communicating hydrocephalus. *Investig. Radiol.* **39**, 45–55 (2004).
40. Attier-Zmudka, J. et al. Decreased cerebrospinal fluid flow is associated with cognitive deficit in elderly patients. *Front. Aging Neurosci.* **11**, 87 (2019).
41. Siyahhan, B. et al. Flow induced by ependymal cilia dominates near-wall cerebrospinal fluid dynamics in the lateral ventricles. *J. R. Soc. Interface* **11**, 20131189 (2014).

Acknowledgements

This work was supported by grants from the St Baldrick Foundation, the Hero-Up Foundation in memory of Keith, and a crowdfunding campaign in memory of Zach. They are both greatly missed. Morgann R. Turkot helped with experimental design and technical expertise. Robert E. Brown helped by staining samples for slide scanning. Lisa Price helped conduct the statistical review of the manuscript.

Author contributions

A.G.A., C.K., S.V.R., B.A.M., D.K., M.K., and N.E.B. designed the experiments. A.G.A., S.V.R., D.K., S.H.C., and B.A.M. performed the

experiments. A.G.A., S.V.R., D.K., M.K., C.K., S.C., M.K., B.A.M., B.L.C., S.H.C., and N.E.B. analyzed the results. B.A.M., S.H.C., and M.K. provided materials.

Competing interests

C.K. has or has had sponsored research agreements with Eli Lilly, Roche-Genentech, and Cardiff Oncology, as well as research collaborations with Novartis, and is co-founder of Tio Companies and Teo Therapeutics. Artisan Biopharma is a wholly owned subsidiary of cc-TDI. B.A.M. is an employee of Alcyone Therapeutics and has been a scientific advisory board member for Novoron Biosciences, Alcyone Lifesciences, Anuncia Medical, Chiari and Syringomyelia Foundation, The International Society for Hydrocephalus and CSF Disorders, and The International CSF Dynamics Society. B.A.M. has received sponsored research funding from NIH, NASA, Biogen Inc., Genentech Inc., Voyager Therapeutics Inc., KBR Wyle, Alcyone Lifesciences Inc., and Minnetronix Inc. B.A.M. has served as a consultant to Flux Neuroscience, Genentech, Roche, Minnetronix, SwanBio Therapeutics, Praxis Medicines, Cerebral Therapeutics, CereVasc, InviCRO, Neurosyntec, Behavior Imaging, Anuncia Medical, and Voyager Therapeutics. All other authors declare no competing interests.

Additional information

Supplementary information The online version contains supplementary material available at <https://doi.org/10.1038/s43856-025-00925-4>.

Correspondence and requests for materials should be addressed to Samuel V. Rasmussen or Charles Keller.

Peer review information *Communications Medicine* thanks Pejman Shojaee and the other, anonymous, reviewer(s) for their contribution to the peer review of this work.

Reprints and permissions information is available at <http://www.nature.com/reprints>

Publisher's note Springer Nature remains neutral with regard to jurisdictional claims in published maps and institutional affiliations.

Open Access This article is licensed under a Creative Commons Attribution-NonCommercial-NoDerivatives 4.0 International License, which permits any non-commercial use, sharing, distribution and reproduction in any medium or format, as long as you give appropriate credit to the original author(s) and the source, provide a link to the Creative Commons licence, and indicate if you modified the licensed material. You do not have permission under this licence to share adapted material derived from this article or parts of it. The images or other third party material in this article are included in the article's Creative Commons licence, unless indicated otherwise in a credit line to the material. If material is not included in the article's Creative Commons licence and your intended use is not permitted by statutory regulation or exceeds the permitted use, you will need to obtain permission directly from the copyright holder. To view a copy of this licence, visit <http://creativecommons.org/licenses/by-nc-nd/4.0/>.

© The Author(s) 2025